A credible homogenized finite element model to predict radius fracture in the case of a forward fall

Martin Revel, Marc Gardegaront, François Bermond, David Mitton, Hélène Follet

A Credible Homogenized Finite Element Model to Predict Radius Fracture in the Case of a Forward Fall.

M. Revel [1, 2], M. Gardegaront [1, 2], F. Bermond [2], D. Mitton [2], H. Follet [1]

[1] Univ Lyon, Univ Claude Bernard Lyon 1, INSERM, LYOS UMR1033, F69008, Lyon, France

[2] Univ Lyon, Univ Gustave Eiffel, Univ Claude Bernard Lyon 1, LBMC UMR_T9406, F69622, Lyon, France

***Corresponding author**:*

Hélène Follet

Univ Lyon – INSERM, UMR1033

Faculté de Médecine Lyon Est -Domaine Laennec-6th

7-11, rue G. Paradin

69372 Lyon cedex 08

France

Phone: +33 4 78 78 57 26

E-mail address: helene.follet@inserm.fr

Keywords: Forward Fall, Finite Element Analysis, Fracture Prediction, Radius, Bone strength

Graphical Abstract

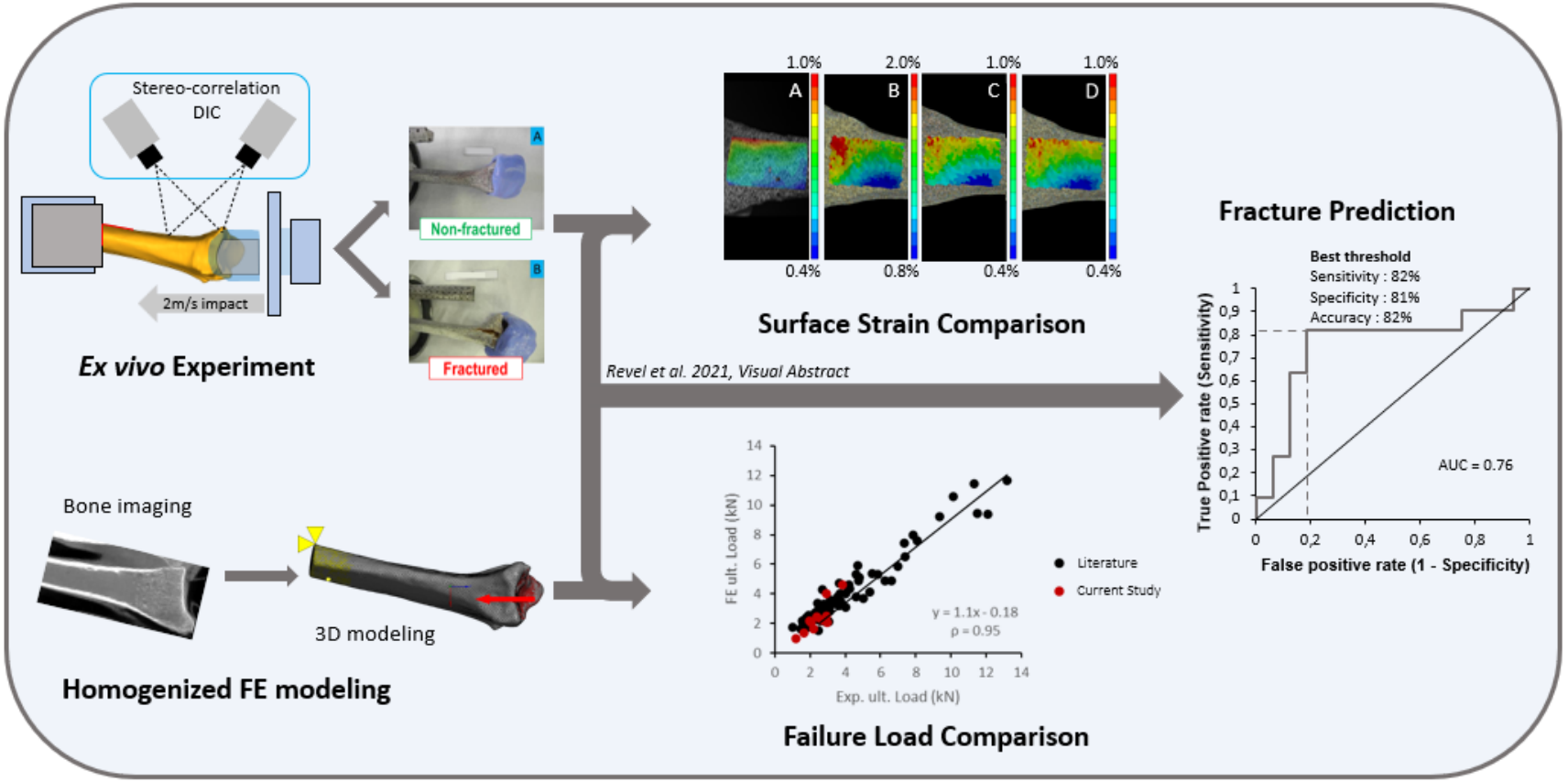

Highlights

- Homogenized finite element models of the radius have been proposed to evaluate bone stiffness, strain and strength
- Elastic-density relationships and failure criterion have an effect on numerical response on distal radius
- Homogenized finite element models of a large region of distal radius can be used to discriminate fractured bones from non-fractured bones

Abstract

Fragility fractures that occur after a fall from a standing height or less are almost always due to osteoporosis, which remains underdiagnosed and untreated. Patient-specific finite element (FE) models have been introduced to predict bone strength and strain. This approach, based on structure mechanics, is derived from Quantitative Computed Tomography (QCT), and element mechanical properties are computed from bone mineral densities. In this study, we developed a credible finite element model of the radius to discriminate low-trauma-fractured radii from non-fractured radii obtained experimentally. Thirty cadaveric radii were impacted with the same loading condition at 2 m/s, and experimental surface strain was retrieved by stereo-correlation in addition to failure loads in fracture cases. Finite element models of the distal radius were created from clinical computed tomography. Different density-elasticity relationships and failure criteria were tested. The strongest agreement (simulations-experiments) for average strain showed a Spearman's rank correlation (ρ) between 0.75 and 0.82, $p < 0.0001$, with a root mean square error between 0.14 and 0.19%. The experimental mean strain was 0.55%. Predicted failure load error (23%) was minimized for derived Pistoia's failure criterion. Numerical failure demonstrated area under the receiver operating characteristic (ROC) curves of 0.76 when classifying radius fractures with an accuracy of 82%. These results suggest that a credible FE modeling method in a large region of interest (distal radius) is a suitable technique to predict radius fractures after a forward fall.

1 Introduction

Fragility fractures represent a worldwide health problem in the elderly (65 years and older) and remain underdiagnosed and untreated [1,2]. Occurring after a fall from standing height or lower (considered as low trauma fractures), radius fractures are the most common upper extremity fractures [3]. These fractures are associated with age-related decline in bone quality, and because they occur earlier in life than other osteoporotic fractures, they can be interpreted as a warning signal for later and more deleterious fractures [4].

Subject-specific finite elements models have been proposed to evaluate bone strength and strain, and fracture risk. Currently, the most widely used tool in clinical research is High Resolution peripheral Quantitative Computed Tomography (HR-pQCT). Based on a restricted area of approximately 9 mm length of the radius (located 9.5 mm to 18.5 mm proximal to the endplate of the radius), micro-finite element (μFE) analysis [5–10] can be performed to assess quasi-static axial bone strength. These μFE models showed good prediction (R^2 between 0.73 and 0.92) when comparing numerical outcomes with quasi-static experimental data [11]. However, despite this good level of prediction, retrospective [4,5,8,12–14] and prospective [15–17] cohort studies have not been able to establish better prediction of fracture risk with μFE analysis compared to the standard reference for the detection of osteoporosis fracture, which is the measurement of areal Bone Mineral Density (aBMD) by Dual X-ray Absorptiometry (DXA). It is only with the BoMIC consortium study, including participants of eight cohorts, that μFE outcomes associated with femoral neck aBMD improved the ability to predict non-traumatic or traumatic incident fracture by enhancing the area under the receiving operating characteristic (ROC) curve ($p < 0.05$) [18]. Nevertheless, this was not the case when considering only major osteoporotic fractures (low-

79 trauma fractures) or when compared μFE outcomes with ultra-distal radius aBMD [18].
80 Radius bone strength through axial quasi-static load is associated with incident fractures, but
81 despite perfectly predicted bone strength, fractures cannot be accurately predicted [11],
82 since fractures in the distal radius mainly result from a fall from a standing height in a
83 forward direction [19,20].

84 Our recent study examined the influence of loading conditions (angle of compression or
85 torsion) in μFE models of 9.02 mm of the distal radius [21]. The results suggested that this
86 approach does not provide improvement in classifying *ex vivo* fractured and non-fractured
87 radii within an elderly population. Using soft layers at the cut faces of the HR–pQCT scanned
88 section, Christen et al. [22] showed that axial loading on the wrist induced axial and shear
89 forces as well as torsion and bending moment on the scanner's region of interest. These
90 authors also showed that physiological bone loading conditions on the cross–section were
91 patient-specific and need a full distal radius scanned region for the determination of realistic
92 load transfer to the scanned region, which is not currently feasible *in vivo* with HR–pQCT. For
93 this reason, we suggest that enlarging the scanning region may facilitate observation of
94 loading sensitivity and reproduction of the *in vivo* mechanism occurring during a fall that led
95 to fracture.

96 Other types of radius FE models have been proposed in a larger region of interest with a
97 homogenized finite element analysis [9,10,23–25]. The accuracy of these homogenized FE
98 (hFE) models is heavily dependent on material properties, boundary conditions, and chosen
99 failure criterion that define fracture threshold [24,25]. However, their use have faded since
100 the introduction of the HR-pQCT μFE during the decade of 2000-2010. Indeed, although hFE

models have predicted bone stiffness, strain, or fracture strength obtained from static experimental tests, they have never been used to predict incident fracture occurring after an impact on the radius resulting from a forward fall on a given population.

Strain rate, in quasi-static constant displacement rate or impact loading, are important considerations for the mechanical behavior of the bone. Compact bovine bone femur was three to four times more brittle under a dynamic load than under a quasi-static load [26]. Moreover, impact velocity has an influence on trabecular bone strain rate which affects the compressive ultimate stress [27]. On human femoral bone, relationships can be found between impact and quasi-static failure loads. An impact scenario can be extrapolated by quasi-static tests with errors of less than 12% [28]. We thus hypothesized that a quasi-static homogenized subject-specific finite element model of the distal radius could, with a different scanner modality than usually used on this site, predict bone fracture following a forward fall.

To confirm this hypothesis, this study aims to propose a credible finite element model to discriminate fractured and non-fractured radius groups obtained experimentally after a forward fall [29]. The credibility of the model was assessed regarding the surface strains field in specific areas and for failure load prediction. The model sensitivity was assessed in terms of the elasticity-density equation and failure criterion.

2 Materials and Methods

2.1 Specimens and Image Acquisition

Data were acquired from 30 fresh-frozen cadaveric left radii from elderly donors (50-96 y.o.; 15 males, 15 females) provided by the University Department of Anatomy Rockefeller (Lyon, France) and were considered for this study (French Ministry of Education and Research, authorization n°DC-2015-2357). The most distal portion of the bones cleaned of soft tissues were imaged with a clinical CT scanner (New-Tom 5G, QR, Verona, Italy). The New-Tom 5G device was chosen for its good spatial resolution in the spectrum of a dental cone beam CT with a nominal detector resolution of 127 µm x 127 µm. Images were acquired on a segment of 8 cm length in the longitudinal direction beginning at the distal styloid of the radius using the standard protocol proposed by the manufacturer, with a tube voltage of 110 kVp and adaptive mAs. Acquisition time was 24 s with an effective dose of approximately 10 µSv (mean radiation dose (CTDI) = 12.6 mGy). Images were reconstructed with a field of view of 8.16 cm and a matrix of 544×544 to give a reconstructed isotropic voxel size of 150 µm.

Scans of the thirty specimens were made along with a forearm calibration phantom (QRM, Moehrendorf, Germany), with calcium hydroxyapatite equivalent concentrations of 0 and 200 mg/cm^3. These scans were used to establish the following linear relationship (i) between CT Hounsfield units (HU) and calcium hydroxyapatite equivalent density ρ_{HA} in g/cm^3:

$$\rho_{HA} = 0.00038 \times HU - 0.1262 \qquad \text{(i)}$$

Each radius was wrapped in saline-moistened gauze and frozen at $-20°C$ before the experiments.

2.2 *Ex-vivo* Experiment

The experimental protocol used here was previously described in detail by Zapata et al. [29]. The day before the experiments took place, bones were thawed for 16 h at 4°C and then 6 h at room temperature. Using a positioning laser, radii were potted with an 8 cm free length in a polyurethane resin in a steel cylinder with an angle of 75±2° between the anterior face of the radius and the impactor. This position reproduces the most common orientation in a forward fall [30]. A rigid polyurethane mold was made to reproduce a simplification of the radio-carpal joint, which is involved in the fracture mechanism [24,25], in order to evenly distribute the load on the articular surface of the radius throughout the impact.

In order to limit the loading of the radius so as to avoid having bone fracture in all cases, the potted bones were placed in a cylinder bar on a rail system, which was free to slide along the loading axis. The weight of the bar (12.5 kg) was considered as an arbitrary weight to represent the mass involved during a fall. This mass was identical for all the tests. A six-axis sensor (105515TF, Humanetics, Germany) was tightened to the impactor located in front of the rail system. The radii were then loaded through the resin mold at 2 m/s using a hydraulic high-speed testing machine (LF technologies, France). The initial distance between the impactor and the mold was 50 mm which allowed the acceleration of the impactor and stabilization of its speed to reach 2 m/s before impact. The displacement of the stroke was set to 10 mm before stops.

Two laser scan acquisitions were made for each specimen. The first laser scan was made on the articular mold at the surface in contact with the articular surface of the radius. This procedure was performed before fixation of the articular mold on the radius using a silicon

rubber (Figure 1-A). The second laser scan corresponds to the whole radius after positioning the pot into the cylinder, just before the impact (Figure 1-B). These two laser acquisitions were useful for the finite element model to retrieve specific loading surface on the radius and specific orientation at the beginning of the experiments.

Observations were recorded using four high-speed cameras (FASTCAM SA3, Photron, Japan) at 2 000 frames per second using a shutter speed of 50 µs with a resolution of 1024 x 1024 pixels (~24 pixel/mm). The cameras were placed in pairs with an angle of 30° (Figure 1-C) and with a distance to specimen of approximately 540 mm. The front cameras, facing the ulnar surface of the radius, recorded the test using 105 mm F2.8 DG Macro sigma lenses. The upper cameras, facing the anterior surface of the radius, recorded the test using 50 mm Z1.4/50 mm ZF planar Zeiss lens. Three spotlights (400D, Dedolight, Germany) provided sufficient lighting to avoid any shadow areas on the images and to ensure good image quality. A speckle was previously painted on the bones to compute strain fields on a specified non-fractured area of the anterior face of the radius (Figure 1-D) by analyzing the video recordings using VIC3D stereo-correlation software (Correlated Solution, South Carolina, USA). A calibration plate was used before each test to re-calibrate the systems for each specimen. The resulting average projection error was ~0.02 pixels. DIC settings were chosen according to manufacturer recommended guidelines: facet size was chosen based on an average valued of ~0.01 pixels of the correlation tracking function (sigma estimate) and resulted to ~41 pixels. Step size (referred to overlap) was roughly a quarter of the subset and resulted to ~10 pixels. The noise through time between consecutive images was measured with respect to the reference image. Thus, a time smothering filter was applied (More detailed information about DIC-settings are provided in Supplementary Table 1).

All samples were impacted under the same loading conditions leading to two groups: fractured and non-fractured radii.

2.3 FE Model

Models of the radii based on segmented CT data from the open-source platform 3D Slicer [31] were imported into Ansys Software (v. 2019 R1 Ansys® Inc., USA) to be meshed (10-nodes, tetrahedra) and to perform the numerical analysis. These continuum meshes were created respecting the quality recommendations on the distortion of the elements by inspecting three parameters: aspect ratio, angle idealization, and element Jacobians [32]. In order to determine the optimal number of elements for the resolution, a mesh convergence study was carried out on a sub-sample of 6 specimens (3 men and 3 women) ranging from 50 000 to 600 000 elements by increments of 50 000. Two parameters were evaluated: mean equivalent von Mises strain in a region of interest of the anterior face of the radius and the maximum von Mises stress in the whole model excluding edge effects (excluding the 5% of the highest stress values). The convergence of the model was considered when the output parameters showed less than a 2% difference between three successive iterations and finally resulting in 200 000 elements, leading to a mean-size element of 0.9 mm edge-length (Supplementary Material).

In order to evaluate the influence of elastic property on the FE models, three previously established relationships were investigated (Eqs. (1)-(3)) to assign inhomogeneous elastic material properties to the FE models (Bonemat v3, [33]). Eq. (1) was developed by Keller *et al.* on lumbar vertebrae and femoral metaphyses and diaphyses [34], Eq. (2) was developed by Morgan *et al*. on femoral neck [35], and Eq. (3) was obtained by Duchemin *et al.* on human cortical femur [36].

$$E = 10\,500\rho_{ash}^{2.57} \quad [34], \quad (1)$$

$$E = 6\,850\rho_{app}^{1.49} \quad [35], \quad (2)$$

$$E = 10\,095\rho_{HA} \quad [36], \quad (3)$$

where Young's modulus E is expressed in MPa, and the densities in g/cm^3, ρ_{ash} (ash density), ρ_{app} (apparent density), and ρ_{HA} (hydroxyapatite equivalent density, obtained with Eq. (i)). Calcium hydroxyapatite equivalent density obtained from the calibration was converted to ash density using:

$\rho_{ash} = 0.0698 + 0.839\ \rho_{HA}$ [37].

Ash density was normalized to apparent density with a ratio of 0.6 between ρ_{ash} and ρ_{app}, within the range 0.55–0.63 identified in the literature [38,39]. This resulted in around 220 materials ranging from 0.05 to 12.1 GPa for Eq. (1), from 0.01 to 15.7 GPa for Eq. (2), and from 0.03 to 12.0 GPa for Eq. (3) (Figure 2). Each element was assigned a Poisson's ratio of 0.3.

The models were specifically oriented in the same configuration as the experiments (with an uncertainty of ±2°) by matching surfaces between the laser scan acquisition and the FE model. The specific maximal peak load observed experimentally was applied to the articular surface along the z axis and the proximal end of the radius at the location of potting was fully constrained (Figure 3). Analysis were performed into Ansys Software (v. 2019 R1 Ansys® Inc., USA).

Three numerical failure criteria were evaluated in this study in order to assess their sensitivity to discriminate fractured bones from non-fractured bones. These criteria have shown good prediction of quasi-static radius [24,40] and femoral [36] failure load. An

element failure occurred when a criterion is greater than or equal to 1 (Table 1). Effective strain based on *Pistoia et al.* was calculated from the strain-energy density (U) and the Young's modulus E of each element: $\varepsilon_{eff} = \sqrt{\frac{2U}{E}}$ with a compressive yield strain (ε_{yc}) set to 0.7% [40]. As inexistant on radius, the maximal von Mises stress and Mohr-Coulomb theories were based on compressive (σ_{yc}) and tensile (σ_{yt}) yield strengths calculated from hydroxyapatite equivalent density using pre-established equations on femoral cortical bone:

$$\sigma_{\mathrm{yc}} = \sigma_{\mathrm{yt}} = 137 \times (1.034 \times \rho_{HA} + 0.0546)^{1.88} \quad \text{for} \quad 0 < \rho_{HA} \leq 0.35 \quad [38,41]$$

$$\sigma_{\mathrm{yc}} = 96.9 \times \rho_{HA} - 5.95 \quad \text{and} \quad \sigma_{\mathrm{yt}} = 64 \times \rho_{HA} - 21.82 \quad \text{for} \quad \rho_{HA} > 0.35 \quad [36,41]$$

Failure loads were then back calculated, assuming that fracture occurred when a cluster of contiguous yielded elements exceeded a predefined volume. Different failed volume has been proposed in the literature: approximatively 150 mm^3 for micro finite element models [40] to 350 mm^3 for homogenized FE models [24,25,42] of the distal radius. A variation of defective volumes ranging from 150 to 450 mm^3 in increments of 100 mm^3 was thus examined. The numerical failure forces obtained for each case was then integrated into the sensitivity study for the detection of fractures.

2.4 Data Analysis

2.4.1 Surface Strain Comparison

Experimental surface strain field was evaluated at the experimental measured peak force for non-fractured bones. The areas from the digital image correlation (DIC) were matched with the surface of the FE models by a custom iterative closest point approach developed in our

laboratory in order to compare the bone numerical response with the experimental data analyzed by stereo-correlation. Principal surface strains measured at peak force were retrieved. Points where the confidence interval σ (a measure for how accurately the displacement of each point is calculated between subsequent images [43]) exceeded 0.02 pixels were excluded before the point-by-point comparison with the numerical model [44].

The following data comparison was developed according to published procedures on femur [44,45]. A sphere, with a diameter of 1.0 mm, was calculated relative to the barycenter of each element of the analyzed surface meshed. All DIC strain measurement points within the sphere were averaged, and the obtained value was used for comparison to the FE element strain. In addition to a visual analysis, the minor and major principal strains were compared by performing a linear regression analysis and calculating the coefficient of determination (R^2), the root mean squared error of estimate (RMSE), and the maximum error (Max err; maximal absolute difference between experimental and numerical values). Dispersion was evaluated using Bland-Altman plots [46]. Analysis was performed for each density-elasticity relationship considered in the current study.

To assess the influence of the ±2° uncertainty during model alignment, the average value of the Von Mises strain was also computed and compared to the experimental values.

2.4.2 Failure Load Comparison

The experimental reaction load curves over time were recorded to retrieve the maximum load of each fractured specimen during the impact. The obtained failure loads were compared with the simulations for each density-elasticity relationship and failure criteria. Due to the limited number of samples, non-parametric statistical tests were performed for this analysis

by calculating Spearman's rank correlations ρ, RMSE, and Max err. The dispersion between these values was evaluated using Bland-Altman plots [46].

2.4.3 Fracture Prediction

Bone fracture was assessed by using the high-speed recordings, but also by a radiologist who interpreted radiographs after the impact. The medians, min, and max of numerical failure loads were calculated. The difference between the fractured and non-fractured bone maximum loads was evaluated using an unpaired Mann-Whitney U test. The small number of samples in each gender did not allow for a separation between males and females for the fracture discrimination analysis, even if significant differences were found between sexes.

A sensitivity/specificity analysis was performed by plotting Receiver Operating Characteristics curves (ROC curves) with their area under the curve (AUC) to determine the optimal threshold for each outcome. This optimal threshold was defined as the furthest point of the curve from the diagonal corresponding to the maximum of the sensitivity + specificity index. For each optimal detection threshold, test accuracy was calculated as the ratio of true positives (TP) and true negatives (TN), divided by the number of samples ($\frac{TP+TN}{n}$). An analysis of variance was carried out on the AUCs compared to 0.5 in order to test whether each diagnosis test was more efficient than a simple random rule [47] and to evaluate the statistical differences between AUCs from the different density-elasticity relationships and failure criteria [48]. All tests were carried out using R software (R Foundation for Statistical Computing, Austria [49]).

3 Results

3.1 Experiments

Among the 30 radii, the experiments failed for two specimens due to misalignments of the potted bones, and the fracture was uncertain for an additional specimen. Finally, 27 bones were tested successfully. As described in the previous study [29], 11 had fractures (7 women, 4 men) after impact and 16 did not fracture (5 women, 11 men). The age of the samples with fractures (Median [Min-Max]: 78 [50-98] years) did not differ significantly from those without fractures (83 [57-96] years) ($p = 0.66$). In contrast, although fractures were not consistently associated with weaker reaction forces, a significant difference was found between the two groups (fractured: 2.38 [1.18 - 3.83] kN, non-fractured: 3.8 [1.69 - 6.27] kN, Difference: -37.3%, $p < 0.01$), regardless of gender.

3.2 Strain Comparison

The minor and major principal strains corresponding to the maximum experimental load were evaluated for each specimen and compared with the predicted strains of the finite element simulation. The sixteen non-fractured bones were considered for the first model evaluation. FE predicted major and minor principal strains had a strong correlation with the experimental measured strains (Figure 4) with $R^2 = 0.76$ for Eq. (1), $R^2 = 0.78$ for Eq. (2) and $R^2 = 0.77$ for Eq. (3). The slope of the linear regression was 1.06 for Eqs. (2)-(3) and 2.77 for Eq. (1). Moreover, Bland-Altman plots showed a bias of 0.27%ε for Eq. (1) with a ±2×SD of 1.73%ε and a bias of almost zero for Eqs. (2) and (3) with a ±2×SD of ~0.40%ε.

In term of Von Mises strain average, the finite element predicted that strains vary as a function of Eqs. (1)-(3) (Figure 5). No significant difference was found between Eq. (2) and

312 (3) ($p > 0.05$) predicting more accurately the experimental values for non-fractured bones
313 than Eq. (1), which overestimates the results. The ±2° uncertainty showed a variation of
314 ±0.08% for Eqs. (2) and (3) and ±0.18% for Eq. (1) in the von Mises strain values. Correlation
315 coefficients for experimentally measured strains versus predicted strains ranging from ρ =
316 [0.68-0.71] ($p < 0.01$) for Eq. (1), to ρ = [0.75-0.82] ($p < 0.001$) for Eq. (2) and ρ = [0.78-0.79]
317 ($p < 0.001$) for Eq. (3) (Table 2). The RMSE and Max Error were smallest for Eqs. (2) and (3)
318 and largest for Eq. (1) (Table 2). Qualitatively, similar results were found in the von Mises
319 spatial strain distribution for the three equations with the min and max values of each field
320 located at the same area. Furthermore, patterns present common characteristics with the
321 experimental fields (Figure 6).

322 ### 3.3 Failure Load Comparison

323 The eleven fractured bones were considered for the second model evaluation. The ±2°
324 uncertainty was no longer considered with regard to the few effects on the surface von Mises
325 strain for Eqs. (2) and (3). The numerical failure load varied as a function of Eqs. (1)-(3),
326 failure criterion, and failure volumes (Figure 7). For the von Mises stress and Mohr-Coulomb
327 criterion, where ultimate strength relied on hydroxyapatite equivalent density, computed
328 failure loads increased with contiguous failed volumes. The lowest RMSEs were found for a
329 volume of 450 mm^3 failed elements for these two criteria (ranging from 895 to 1181 N,
330 corresponding to an error of 37 to 49% of the mean failure force measured experimentally).
331 Max error was smallest for Eq. (1) and largest for Eq. (2) (Supplementary Material).
332 Regarding the effective strain criterion based on Pistoia et al. [40], a fixed threshold of 0.7%
333 strain leads to lower error for Eqs. 2 and 3. With this given criterion, the lowest RSME (558
334 N), max relative error (999 N), and average differences (-51 N) were found for a contiguous

failed volume of 250 mm^3 and Eq. 2 corresponding to a mean error (RMSE%) of 23%. The Effective strain criterion, with a contiguous failed volume of 250 mm^3 and the density-elasticity equation 2, was considered in the rest of the study.

The correlation coefficient for experimentally measured failure load versus predicted failure load was $\rho = 0.74$ ($p = 0.01$). Data was compared with the literature to see if the results were part of a larger population. The radius failure loads of three different validated FE models with continuous meshing were extracted with their respective experimental data [9,23,50] and plotted in Figure 8. These studies have shown good agreement between quasi-static experimental tests and FE analysis (R^2 = 0.87 [23], R^2 = 0.93 [50] and R^2 = 0.95 [9]). For an easier comparison with the literature results, the coefficient of determination was calculated for the current study (R^2 = 0.73, $p < 0.05$). Computed failure loads of the current study were in good agreement with the literature and can confirm good results for a larger population (Figure 8).

3.4 Fracture Prediction

A significant difference was found between experimental fractured and non-fractured bones maximum loads ($p < 0.05$). Median, min, and max are summarized in Table 3. A sensitivity/specificity study was performed by plotting ROC curves (Figure 9). The area under the curve (0.76) was significantly different from a random rule. An optimal threshold of detection was found with a sensitivity of 82% and specificity of 81%. This threshold allowed an accuracy of 82% for radius fracture prediction by subject-specific FE analysis in the case of a forward fall.

4 Discussion

This study investigated whether radius hFE modeling based on clinical imaging on a large distal area could discriminate *ex vivo* fractured bones from non-fractured bones. The model development required a sensitivity analysis on parameters such as the relation between the image grey level and elastic properties as well as failure criterion. The credibility of the model was assessed by comparing experimental and numerical surface strains and failure loads. This is the first study to use enlarged distal radius hFE modelling to discriminate fractured from non-fractured bones.

Strain values in specific areas were similar between numerical simulations and experimental analysis on non-fractured bones for Eqs. (2) and (3) ($R^2 = 0.77$, $p < 0.001$, quadratic error of 21%ε with a slope of 1.06 for the principal strains. Spearman's ρ between 0.75 and 0.82, $p < 0.0001$, quadratic error between 0.14 and 0.19%ε with a slope of ~1.0 for the average Von Mises strain). These results illustrate that experimental surface strains (induced by an impact at 2 m/s) in specific area in elastic response can be correctly predicted by quasi-static simulations. A point-by-point comparison (Figure 4) is given for the first time on the radius. Such a comparison was proposed on the femur [44,45] and even if a direct comparison cannot be done, the current results are in the same range (e.g., slope of the regression and mean values of the difference between simulated and experimental strains).

Literature showed that bone mechanical behavior is strain rate dependent. However, it is not a standard practice to use strain as a trustworthy parameter and the authors rather investigated the strain rate influence on stress or failure loads [28]. The authors have investigated the mechanical properties of cancellous bone (including strain) from quasi-

static to dynamic strain rates with an emphasis on the intermediate regime [51]. The authors showed that within different regimes with a distinct strain rate from 0.001/s to 600/s, the yield stress and apparent modulus were strain rate dependent (significantly higher with higher strain rate). However, no significant difference was found for yield strain, suggesting that strain in elastic region is not greatly influenced by strain rate. The same results were found for the cortical bone [52]. These results suggest that strain should be similar between quasi-static and dynamic loadings.

The strong variation found for Eq. (1) illustrated the sensitivity of the model to the density-elasticity relationship. Because many of these equations exist in the literature [53], particular care should be made when developing a subject-specific finite element model. Some studies have investigated the influence of the density–elasticity relationship on the accuracy of specimen-specific finite element predicted strains [24,54,55]. Edwards and Troy [24] compared three density–elasticity relationships for the human radius under quasi-static axial loading and found that Eq. (1) of the present study [34] showed the best agreement between numerical and experimental surface strains. Nonetheless, this relationship provided the poorest agreement between experimental and predicted surface strains in the present study. The most notable differences with the present study occurred between experiments. When Edwards and Troy loaded the radius axially through carpal bone and ligament at a low strain rate, the present study impacted the bones through a simplification of the radio-carpal joint at a high strain rate. This confirms that bone response is heavily dependent on boundary conditions such as the strain rate [56,57] or loading transfer [25]. Schileo et al. [54] also compared three density–elasticity relationships, although in human femurs, under several loading orientations and observed that Eq. (2) of the present study produced the best results.

401 On the human ulna, Austman et al. [55] tested six different density–elasticity relationships
402 under a simplified cantilever bending scenario and found the best agreement between
403 numerical and experimental data for the two relationships from Carter and Hayes [56], which
404 are not used in this study, and the pooled bone site relationship described by Morgan et al.
405 [35] with Eq. (2). The differences in accuracy between studies confirmed the dependance of
406 anatomical site [35] and boundary conditions [25,42,56] of the density-elasticity
407 relationships on model accuracy.

408 The current study suggested that the effective strain criterion based on Pistoia et al. [40] and
409 currently used in μFE HR-pQCT analysis produced the best agreement ($\rho = 0.74$) with the
410 lowest amount of error (23%). But the small number of samples did not allow observation of
411 whether the FE method of the current study could be applied to an enlarged population.
412 Similar *in vitro* studies showed agreement with the squared Pearson's R^2 ranging from 0.72
413 to 0.95 [9–11,23,24,50,58], depending on the number of specimens, constitutive law, loading
414 scenario(s), model meshing technique (voxel vs. geometry based), and failure criterion.
415 When available and with similar modelling approaches, failure loads from the literature were
416 extracted and compared with the results of the current study. These data compared quasi-
417 static numerical failure load with low strain rate experimental loading until fracture. Despite
418 strain rate and impact influencing the mechanical behavior of the bone [26–28,59], the
419 fracture loads of the current study were added to the scatter plots of the literature to see
420 their position in an enlarged population and show the credibility of the model before looking
421 at fractures discrimination. Computed failure loads of the current study were in good
422 agreement with the literature even if values were in the lower side of the range. However,
423 conflicting results have been reported on femurs regarding the effect of the displacement

rate. Similar studies show that with a higher displacement rate the fracture load should increase [28,60]. An increased fracture load could also be expected for the radius. Thus, the fracture loads of the current study should have been in the upper range of the Figure 8, including studies performed in quasi-static conditions. However, other parameters will affect the fracture loads, such as sex, age, size of the bone, bone mineral density, and orientation of the loading. In Figure 8, the results from Hosseini et al. 2017 [9] present the highest values. The failure loads were obtained on radius sections (pure compression) from younger subjects (77.5±9 y.o.) compared to other studies (81±10 y.o. for [23], 81±14 y.o. for [50], and 79.7±13 y.o. for the current study) and with a larger proportion of males. This may explain the larger values for that study. Moreover, the results from these studies were obtained on distal radius loaded in the direction of the diaphysis axis ("pure compression"). On the contrary, the current study considered an angle between the loading direction and the diaphysis axis. This loading configuration reduces the failure load compared to the loading in "pure compression". This important difference is probably the major reason why the failure loads in the current study are in the lower range of the failure loads reported in Figure 8, despite the impact loading. The majority of the fractured bones of the current study was considered osteoporotic by ultra-distal radius aBMD (DXA) [29]. This information was not available in the other studies. These low bone mineral densities might also explain the position of the current specimens compared to the literature. This comparison therefore highlighted that a sample size of 11 specimens for model validation is limited and this kind of analysis needs a larger population to confirm accuracy. However, the results suggested that the quasi-static hFE models of the distal radius can predict failure load obtained after an impact on the joint surface.

Computed failure loads on the current study computed by hFE analysis were associated with incident fracture. Predictions of HR-pQCT μFE and DXA measurement on the same pool of experimental data were previously established [21]. Derived μFE parameters showed an AUC of 0.795 with 82% accuracy for fracture detection of the best threshold (Sensitivity: 73%, Specificity: 88%). The DXA aBMD of the distal radius presented statistical similar results with an AUC of 0.773 and 85% accuracy (Sensitivity: 82%, Specificity: 88%) [21]. The current model showed similar fracture prediction and was comparable to the technique used in the clinical research. If DXA has little room for progress, as well as μFE, limited by acquisition *in vivo* and restricted area, the hFE analysis with a clinical scan at a lower resolution has a large field of improvement. For further development, an enlarged distal radius FE model would allow more complex boundary conditions compared to a restricted area (e.g., different loading cases occurring *in vivo*). With this type of modelling, a full wrist FE model is conceivable with the presence of carpal bone, cartilage, and tendons which can apply stress to the bone. Moreover, we determined that the numerical response depends on density-elasticity relationships; no such type of relationship was developed specifically for the distal radius. Its development in fall conditions should help improve FE model accuracy. Inclusion of strain-rate-dependent behavior in our model, which could be done for Young's modulus by including a second power term in the density–elasticity relationship [56], could be also done to best fit the experimental conditions. Our group showed in a comparative study that the cortical bones from the radius and the femur present the same toughness under a strain rate representative of a fall [59]. This suggests that similar behavior for both sites is expected in the case of a fall-loading condition.

There are some limitations in the current study. First, the small sample consisted of 15 men and 15 women. Most of the non-fractured bones came from male donors, while the majority of fractured bones came from female donors [29], which may induce a bias during the sensitivity analysis. Moreover, the small number of samples did not allow for the possibility of full proper model validation, which requires a larger number of specimens. This problem was partially solved using previous published studies found in the literature, but different modelling techniques or experimental conditions remain present in these experiments. Analyses of a larger number of single-sex samples would eliminate this bias. Other limitations are related to the use of cadaveric samples. Like most *ex vivo* studies on bones, the specimens were frozen, which is considered the best conservation mode. Moreover, the articular joint is simplified, and the load was evenly distributed on the articular surface of the radius while carpal bones have an effect on radius bone strength [25]. These simplifications differ from the *in vivo* phenomenon occurring during a fall in which soft tissue, ligament, and carpal bones are present and transfer the load to the radius.

5 Conclusions

Quasi-static hFE simulations could predict the elastic deformations of an external surface of the radius during dynamic experiments of forward falls on the forearm and depend on density-elasticity relationships. Failure criterion adapted from Pistoia et al. [40] was added to the linear elastic constitutive law to predict distal radius failure load. The originality of the current study is related to the evaluation of a homogenized finite element model to discriminate the two groups of bones (fractured and non-fractured) obtained through a

unique loading condition. These results suggest that a credible FE modeling method is a suitable technique for predicting radius fractures occurring after a forward fall.

Acknowledgements

The authors would like to thank Karine Bruyère-Garnier for her help for the use of Vic3D.

Conflict of interest

There is no conflict of interest for any of the authors.

References

[1] S. Khosla, E. Shane, A Crisis in the Treatment of Osteoporosis, J. Bone Miner. Res. Off. J. Am. Soc. Bone Miner. Res. 31 (2016) 1485–1487. https://doi.org/10.1002/jbmr.2888.

[2] C. Roux, K. Briot, Osteoporosis in 2017: Addressing the crisis in the treatment of osteoporosis, Nat. Rev. Rheumatol. 14 (2018) 67–68. https://doi.org/10.1038/nrrheum.2017.218.

[3] M.T. Vogt, J.A. Cauley, M.M. Tomaino, K. Stone, J.R. Williams, J.H. Herndon, Distal radius fractures in older women: a 10-year follow-up study of descriptive characteristics and risk factors. The study of osteoporotic fractures, J. Am. Geriatr. Soc. 50 (2002) 97–103. https://doi.org/10.1046/j.1532-5415.2002.50014.x.

[4] L.J. Melton, D. Christen, B.L. Riggs, S.J. Achenbach, R. Müller, G.H. van Lenthe, S. Amin, E.J. Atkinson, S. Khosla, Assessing forearm fracture risk in postmenopausal women, Osteoporos. Int. 21 (2010) 1161–1169. https://doi.org/10.1007/s00198-009-1047-2.

[5] S. Boutroy, B. Van Rietbergen, E. Sornay-Rendu, F. Munoz, M.L. Bouxsein, P.D. Delmas, Finite element analysis based on in vivo HR-pQCT images of the distal radius is associated with wrist fracture in postmenopausal women, J. Bone Miner. Res. Off. J. Am. Soc. Bone Miner. Res. 23 (2008) 392–399. https://doi.org/10.1359/jbmr.071108.

[6] D.E. Whittier, S.L. Manske, D.P. Kiel, M. Bouxsein, S.K. Boyd, Harmonizing finite element modelling for non-invasive strength estimation by high-resolution peripheral quantitative computed tomography, J. Biomech. 80 (2018) 63–71. https://doi.org/10.1016/j.jbiomech.2018.08.030.

[7] D.E. Whittier, S.K. Boyd, A.J. Burghardt, J. Paccou, A. Ghasem-Zadeh, R. Chapurlat, K. Engelke, M.L. Bouxsein, Guidelines for the assessment of bone density and microarchitecture in vivo using high-resolution peripheral quantitative computed tomography, Osteoporos. Int. J. Establ. Result Coop. Eur. Found. Osteoporos. Natl. Osteoporos. Found. USA. (2020). https://doi.org/10.1007/s00198-020-05438-5.

[8] N. Vilayphiou, S. Boutroy, E. Sornay-Rendu, B. Van Rietbergen, F. Munoz, P.D. Delmas, R. Chapurlat, Finite element analysis performed on radius and tibia HR-pQCT images and fragility fractures at all sites in postmenopausal women, Bone. 46 (2010) 1030–1037. https://doi.org/10.1016/j.bone.2009.12.015.

[9] H.S. Hosseini, A. Dünki, J. Fabech, M. Stauber, N. Vilayphiou, D. Pahr, M. Pretterklieber, J. Wandel, B. van Rietbergen, P.K. Zysset, Fast estimation of Colles' fracture load of the distal section of the radius by homogenized finite element analysis based on HR-pQCT, Bone. 97 (2017) 65–75. https://doi.org/10.1016/j.bone.2017.01.003.

[10] A.J. Arias-Moreno, H.S. Hosseini, M. Bevers, K. Ito, P. Zysset, B. van Rietbergen, Validation of distal radius failure load predictions by homogenized- and micro-finite element analyses based on second-generation high-resolution peripheral quantitative CT images, Osteoporos. Int. J. Establ. Result Coop. Eur. Found. Osteoporos. Natl. Osteoporos. Found. USA. 30 (2019) 1433–1443. https://doi.org/10.1007/s00198-019-04935-6.

[11] B. van Rietbergen, K. Ito, A survey of micro-finite element analysis for clinical assessment of bone strength: the first decade, J. Biomech. 48 (2015) 832–841. https://doi.org/10.1016/j.jbiomech.2014.12.024.

[12] T. Chevalley, J.P. Bonjour, B. van Rietbergen, S. Ferrari, R. Rizzoli, Fracture history of healthy premenopausal women is associated with a reduction of cortical

microstructural components at the distal radius, Bone. 55 (2013) 377–383. https://doi.org/10.1016/j.bone.2013.04.025.
[13] K.K. Nishiyama, H.M. Macdonald, D.A. Hanley, S.K. Boyd, Women with previous fragility fractures can be classified based on bone microarchitecture and finite element analysis measured with HR-pQCT, Osteoporos. Int. 24 (2013) 1733–1740. https://doi.org/10.1007/s00198-012-2160-1.
[14] N. Vilayphiou, S. Boutroy, P. Szulc, B. van Rietbergen, F. Munoz, P.D. Delmas, R. Chapurlat, Finite element analysis performed on radius and tibia HR-pQCT images and fragility fractures at all sites in men, J. Bone Miner. Res. 26 (2011) 965–973. https://doi.org/10.1002/jbmr.297.
[15] E. Sornay-Rendu, S. Boutroy, F. Duboeuf, R.D. Chapurlat, Bone Microarchitecture Assessed by HR-pQCT as Predictor of Fracture Risk in Postmenopausal Women: The OFELY Study, J. Bone Miner. Res. Off. J. Am. Soc. Bone Miner. Res. 32 (2017) 1243–1251. https://doi.org/10.1002/jbmr.3105.
[16] C. Ohlsson, D. Sundh, A. Wallerek, M. Nilsson, M. Karlsson, H. Johansson, D. Mellström, M. Lorentzon, Cortical Bone Area Predicts Incident Fractures Independently of Areal Bone Mineral Density in Older Men, J. Clin. Endocrinol. Metab. 102 (2017) 516–524. https://doi.org/10.1210/jc.2016-3177.
[17] E. Biver, C. Durosier-Izart, T. Chevalley, B. van Rietbergen, R. Rizzoli, S. Ferrari, Evaluation of Radius Microstructure and Areal Bone Mineral Density Improves Fracture Prediction in Postmenopausal Women, J. Bone Miner. Res. Off. J. Am. Soc. Bone Miner. Res. 33 (2018) 328–337. https://doi.org/10.1002/jbmr.3299.
[18] E.J. Samelson, K.E. Broe, H. Xu, L. Yang, S. Boyd, E. Biver, P. Szulc, J. Adachi, S. Amin, E. Atkinson, C. Berger, L. Burt, R. Chapurlat, T. Chevalley, S. Ferrari, D. Goltzman, D.A. Hanley, M.T. Hannan, S. Khosla, C.-T. Liu, M. Lorentzon, D. Mellstrom, B. Merle, M. Nethander, R. Rizzoli, E. Sornay-Rendu, B. Van Rietbergen, D. Sundh, A.K.O. Wong, C. Ohlsson, S. Demissie, D.P. Kiel, M.L. Bouxsein, Cortical and trabecular bone microarchitecture as an independent predictor of incident fracture risk in older women and men in the Bone Microarchitecture International Consortium (BoMIC): a prospective study, Lancet Diabetes Endocrinol. 7 (2019) 34–43. https://doi.org/10.1016/S2213-8587(18)30308-5.
[19] J. Oskam, J. Kingma, H.J. Klasen, Fracture of the distal forearm: epidemiological developments in the period 1971-1995, Injury. 29 (1998) 353–355. https://doi.org/10.1016/s0020-1383(97)00212-x.
[20] T.W. O'Neill, J. Varlow, A.J. Silman, J. Reeve, D.M. Reid, C. Todd, A.D. Woolf, Age and sex influences on fall characteristics, Ann. Rheum. Dis. 53 (1994) 773–775. https://doi.org/10.1136/ard.53.11.773.
[21] M. Revel, F. Bermond, F. Duboeuf, D. Mitton, H. Follet, Influence of Loading Conditions in Finite Element Analysis Assessed by HR–pQCT on Ex Vivo Fracture Prediction, Bone. (2021) 116206. https://doi.org/10.1016/j.bone.2021.116206.
[22] P. Christen, K. Ito, I. Knippels, R. Müller, G.H. van Lenthe, B. van Rietbergen, Subject-specific bone loading estimation in the human distal radius, J. Biomech. 46 (2013) 759–766. https://doi.org/10.1016/j.jbiomech.2012.11.016.
[23] P. Varga, S. Baumbach, D. Pahr, P.K. Zysset, Validation of an anatomy specific finite element model of Colles' fracture, J. Biomech. 42 (2009) 1726–1731. https://doi.org/10.1016/j.jbiomech.2009.04.017.

[24] W.B. Edwards, K.L. Troy, Finite element prediction of surface strain and fracture strength at the distal radius, Med. Eng. Phys. 34 (2012) 290–298. https://doi.org/10.1016/j.medengphy.2011.07.016.
[25] W.B. Edwards, K.L. Troy, Simulating distal radius fracture strength using biomechanical tests: a modeling study examining the influence of boundary conditions, J. Biomech. Eng. 133 (2011) 114501. https://doi.org/10.1115/1.4005428.
[26] M. Pithioux, D. Subit, P. Chabrand, Comparison of compact bone failure under two different loading rates: experimental and modelling approaches, Med. Eng. Phys. 26 (2004) 647–653. https://doi.org/10.1016/j.medengphy.2004.05.002.
[27] W.S. Enns-Bray, S.J. Ferguson, B. Helgason, Strain rate dependency of bovine trabecular bone under impact loading at sideways fall velocity, J. Biomech. 75 (2018) 46–52. https://doi.org/10.1016/j.jbiomech.2018.04.042.
[28] F. Jazinizadeh, H. Mohammadi, C.E. Quenneville, Comparing the fracture limits of the proximal femur under impact and quasi-static conditions in simulation of a sideways fall, J. Mech. Behav. Biomed. Mater. 103 (2020) 103593. https://doi.org/10.1016/j.jmbbm.2019.103593.
[29] E. Zapata, F. Rongieras, J.-B. Pialat, H. Follet, D. Mitton, An ex vivo experiment to reproduce a forward fall leading to fractured and non-fractured radii, J. Biomech. 63 (2017) 174–178. https://doi.org/10.1016/j.jbiomech.2017.08.013.
[30] J. Chiu, S.N. Robinovitch, Prediction of upper extremity impact forces during falls on the outstretched hand, J. Biomech. 31 (1998) 1169–1176. https://doi.org/10.1016/S0021-9290(98)00137-7.
[31] A. Fedorov, R. Beichel, J. Kalpathy-Cramer, J. Finet, J.-C. Fillion-Robin, S. Pujol, C. Bauer, D. Jennings, F. Fennessy, M. Sonka, J. Buatti, S. Aylward, J.V. Miller, S. Pieper, R. Kikinis, 3D Slicer as an Image Computing Platform for the Quantitative Imaging Network, Magn. Reson. Imaging. 30 (2012) 1323–1341. https://doi.org/10.1016/j.mri.2012.05.001.
[32] T.A. Burkhart, D.M. Andrews, C.E. Dunning, Finite element modeling mesh quality, energy balance and validation methods: a review with recommendations associated with the modeling of bone tissue, J. Biomech. 46 (2013) 1477–1488. https://doi.org/10.1016/j.jbiomech.2013.03.022.
[33] F. Taddei, E. Schileo, B. Helgason, L. Cristofolini, M. Viceconti, The material mapping strategy influences the accuracy of CT-based finite element models of bones: an evaluation against experimental measurements, Med. Eng. Phys. 29 (2007) 973–979. https://doi.org/10.1016/j.medengphy.2006.10.014.
[34] T.S. Keller, Predicting the compressive mechanical behavior of bone, J. Biomech. 27 (1994) 1159–1168. https://doi.org/10.1016/0021-9290(94)90056-6.
[35] E.F. Morgan, H.H. Bayraktar, T.M. Keaveny, Trabecular bone modulus-density relationships depend on anatomic site, J. Biomech. 36 (2003) 897–904. https://doi.org/10.1016/S0021-9290(03)00071-X.
[36] L. Duchemin, V. Bousson, C. Raossanaly, C. Bergot, J.D. Laredo, W. Skalli, D. Mitton, Prediction of mechanical properties of cortical bone by quantitative computed tomography, Med. Eng. Phys. 30 (2008) 321–328. https://doi.org/10.1016/j.medengphy.2007.04.008.
[37] T.S. Kaneko, J.S. Bell, M.R. Pejcic, J. Tehranzadeh, J.H. Keyak, Mechanical properties, density and quantitative CT scan data of trabecular bone with and without metastases, J. Biomech. 37 (2004) 523–530. https://doi.org/10.1016/j.jbiomech.2003.08.010.

[38] J.H. Keyak, I.Y. Lee, H.B. Skinner, Correlations between orthogonal mechanical properties and density of trabecular bone: Use of different densitometric measures, J. Biomed. Mater. Res. 28 (1994) 1329–1336. https://doi.org/10.1002/jbm.820281111.
[39] E. Schileo, F. Taddei, L. Cristofolini, M. Viceconti, Subject-specific finite element models implementing a maximum principal strain criterion are able to estimate failure risk and fracture location on human femurs tested in vitro, J. Biomech. 41 (2008) 356–367. https://doi.org/10.1016/j.jbiomech.2007.09.009.
[40] W. Pistoia, B. van Rietbergen, E.-M. Lochmüller, C.A. Lill, F. Eckstein, P. Rüegsegger, Estimation of distal radius failure load with micro-finite element analysis models based on three-dimensional peripheral quantitative computed tomography images, Bone. 30 (2002) 842–848. https://doi.org/10.1016/S8756-3282(02)00736-6.
[41] L. Duchemin, D. Mitton, E. Jolivet, V. Bousson, J.D. Laredo, W. Skalli, An anatomical subject-specific FE-model for hip fracture load prediction, Comput. Methods Biomech. Biomed. Engin. 11 (2008) 105–111. https://doi.org/10.1080/10255840802297143.
[42] K.L. Troy, M.D. Grabiner, Off-axis loads cause failure of the distal radius at lower magnitudes than axial loads: a finite element analysis, J. Biomech. 40 (2007) 1670–1675. https://doi.org/10.1016/j.jbiomech.2007.01.018.
[43] M.A. Michael A., J.-J. Orteu, H.W. Schreier, Introduction, in: H. Schreier, J.-J. Orteu, M.A. Sutton (Eds.), Image Correl. Shape Motion Deform. Meas. Basic ConceptsTheory Appl., Springer US, Boston, MA, 2009: pp. 1–12. https://doi.org/10.1007/978-0-387-78747-3_1.
[44] J. Kok, L. Grassi, A. Gustafsson, H. Isaksson, Femoral strength and strains in sideways fall: Validation of finite element models against bilateral strain measurements, J. Biomech. 122 (2021) 110445. https://doi.org/10.1016/j.jbiomech.2021.110445.
[45] Y. Katz, Z. Yosibash, New insights on the proximal femur biomechanics using Digital Image Correlation, J. Biomech. 101 (2020) 109599. https://doi.org/10.1016/j.jbiomech.2020.109599.
[46] M.J. Bland, DouglasG. Altman, STATISTICAL METHODS FOR ASSESSING AGREEMENT BETWEEN TWO METHODS OF CLINICAL MEASUREMENT, The Lancet. 327 (1986) 307–310. https://doi.org/10.1016/S0140-6736(86)90837-8.
[47] J.A. Hanley, B.J. McNeil, A method of comparing the areas under receiver operating characteristic curves derived from the same cases., Radiology. 148 (1983) 839–843. https://doi.org/10.1148/radiology.148.3.6878708.
[48] E.R. DeLong, D.M. DeLong, D.L. Clarke-Pearson, Comparing the Areas under Two or More Correlated Receiver Operating Characteristic Curves: A Nonparametric Approach, Biometrics. 44 (1988) 837–845. https://doi.org/10.2307/2531595.
[49] RR Core Team, R: A language and environment for statistical computing, (2013) 16.
[50] P. Varga, E. Dall'Ara, D.H. Pahr, M. Pretterklieber, P.K. Zysset, Validation of an HR-pQCT-based homogenized finite element approach using mechanical testing of ultra-distal radius sections, Biomech. Model. Mechanobiol. 10 (2011) 431–444. https://doi.org/10.1007/s10237-010-0245-3.
[51] M. Prot, T.J. Cloete, D. Saletti, S. Laporte, The behavior of cancellous bone from quasi-static to dynamic strain rates with emphasis on the intermediate regime, J. Biomech. 49 (2016) 1050–1057. https://doi.org/10.1016/j.jbiomech.2016.02.021.
[52] M.J. Katzenberger, D.L. Albert, A.M. Agnew, A.R. Kemper, Effects of sex, age, and two loading rates on the tensile material properties of human rib cortical bone, J. Mech.

682 Behav. Biomed. Mater. 102 (2020) 103410.
683 https://doi.org/10.1016/j.jmbbm.2019.103410.
684 [53] N.K. Knowles, J.M. Reeves, L.M. Ferreira, Quantitative Computed Tomography (QCT)
685 derived Bone Mineral Density (BMD) in finite element studies: a review of the literature,
686 J. Exp. Orthop. 3 (2016) 36. https://doi.org/10.1186/s40634-016-0072-2.
687 [54] E. Schileo, F. Taddei, A. Malandrino, L. Cristofolini, M. Viceconti, Subject-specific finite
688 element models can accurately predict strain levels in long bones, J. Biomech. 40 (2007)
689 2982–2989. https://doi.org/10.1016/j.jbiomech.2007.02.010.
690 [55] R.L. Austman, J.S. Milner, D.W. Holdsworth, C.E. Dunning, The effect of the density–
691 modulus relationship selected to apply material properties in a finite element model of
692 long bone, J. Biomech. 41 (2008) 3171–3176.
693 https://doi.org/10.1016/j.jbiomech.2008.08.017.
694 [56] D.R. Carter, W.C. Hayes, The compressive behavior of bone as a two-phase porous
695 structure, J. Bone Joint Surg. Am. 59 (1977) 954–962.
696 [57] U. Hansen, P. Zioupos, R. Simpson, J.D. Currey, D. Hynd, The Effect of Strain Rate on the
697 Mechanical Properties of Human Cortical Bone, J. Biomech. Eng. 130 (2008).
698 https://doi.org/10.1115/1.2838032.
699 [58] T.A. Burkhart, C.E. Quenneville, C.E. Dunning, D.M. Andrews, Development and
700 validation of a distal radius finite element model to simulate impact loading indicative
701 of a forward fall, Proc. Inst. Mech. Eng. [H]. 228 (2014) 258–271.
702 https://doi.org/10.1177/0954411914522781.
703 [59] R. Gauthier, H. Follet, M. Langer, S. Meille, J. Chevalier, F. Rongiéras, F. Peyrin, D. Mitton,
704 Strain rate influence on human cortical bone toughness: A comparative study of four
705 paired anatomical sites, J. Mech. Behav. Biomed. Mater. 71 (2017) 223–230.
706 https://doi.org/10.1016/j.jmbbm.2017.03.015.
707 [60] A.C. Courtney, E.F. Wachtel, E.R. Myers, W.C. Hayes, Effects of loading rate on strength of
708 the proximal femur, Calcif. Tissue Int. 55 (1994) 53–58.
709 https://doi.org/10.1007/BF00310169.
710

711

Figure List

Table List

Table 1: The failure criterion investigated with their respective equations. $\boldsymbol{\varepsilon_{eff}}$ is the effective strain estimated from the strain energy density [40]; $\boldsymbol{\varepsilon_{yc}}$ the compressive failure strain; $\boldsymbol{\sigma_{vm}}$ the von Mises stress; $\boldsymbol{\sigma_1}$, $\boldsymbol{\sigma_2}$, and $\boldsymbol{\sigma_3}$ are the principal stresses ($\boldsymbol{\sigma_1 > \sigma_2 > \sigma_3}$); and $\boldsymbol{\sigma_{yc}}$ and $\boldsymbol{\sigma_{yt}}$ the compressive and tensile failure stresses.

Criterions	Equations
Effective strain	$\frac{\varepsilon_{eff}}{\varepsilon_{yc}} \geq 1$
Maximal von Mises stress	$\frac{\sigma_{vm}}{\sigma_{yc}} \geq 1$
Mohr-Coulomb	$\frac{\sigma_1}{\sigma_{yt}} - \frac{\sigma_3}{\sigma_{yc}} \geq 1$

*Table 2: Spearman's rank correlation (ρ), RMSE and Maximum error between experimental and numerical means surface strains in non-fracture cases for the three chosen elastic-density relationships Eqs. (1)-(3) considered. *p-value < 0.01, **p-value < 0.001*

	Eq. (1)	Eq. (2)	Eq. (3)
Spearman's ρ	[0.68-0.71]*	[0.75-0.82]**	[0.78-0.79]**
RMSE (%ε)	[0.65-0.98]	[0.14-0.19]	[0.15-0.18]
Max err (%ε)	1.63	0.37	0.36

Table 3: Median [Min - Max] of the numerical failure load among the two fracture groups. The difference between the groups (fractured vs. non-fractured) is given as a percentage relative to the values of the non-fractured with significance corresponding to the Mann-Whitney U test.

Parameters	Non-fractured (n = 16)	Fractured (n = 11)	Difference (%)	p-value
Exp. Maximum Load (kN)	3.80 [1.69 - 6.27]	2.38 [1.18 - 3.83]	-37.4	<0.01
Computed Failure Load (kN)	3.14 [1.34 - 4.70]	2.16 [0.97 - 4.63]	-31.2	0.03

Figure 1

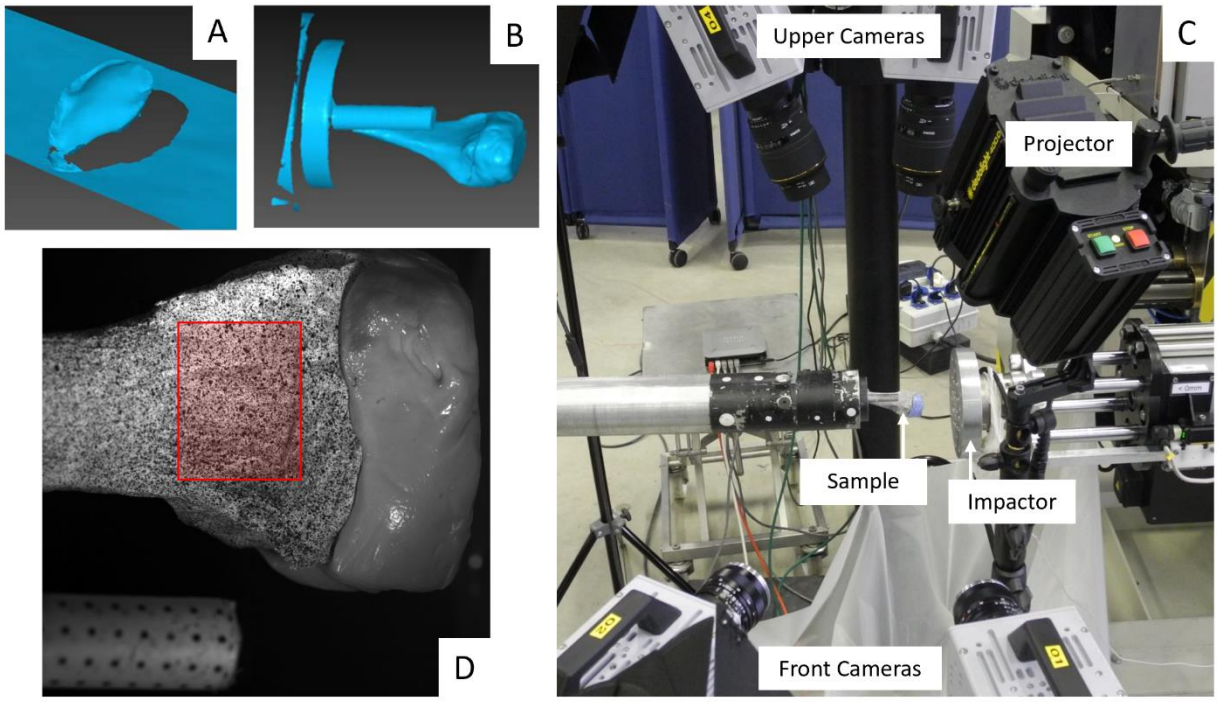

Figure 2

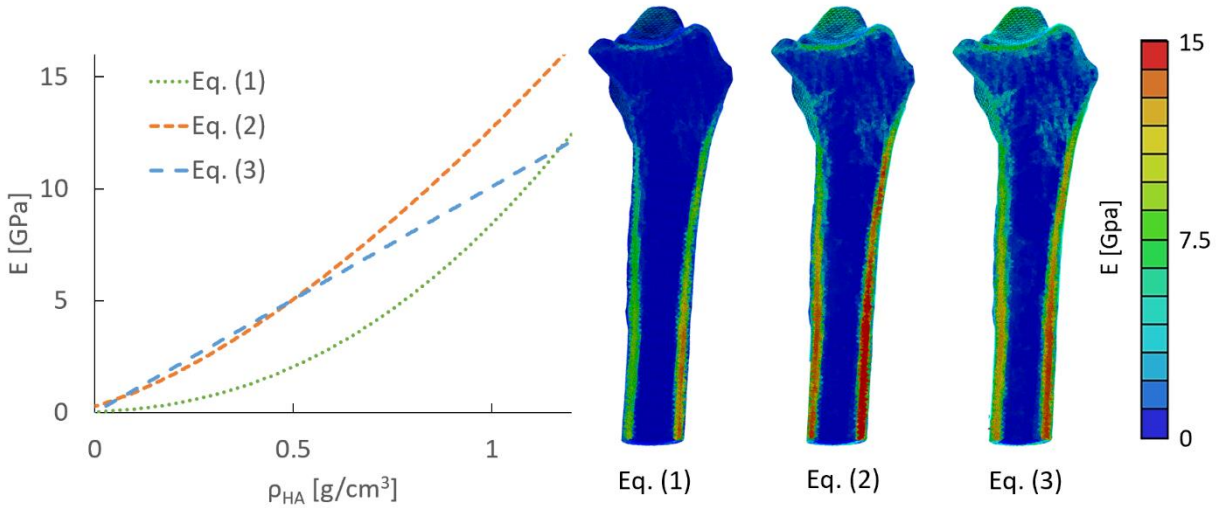

Figure 3

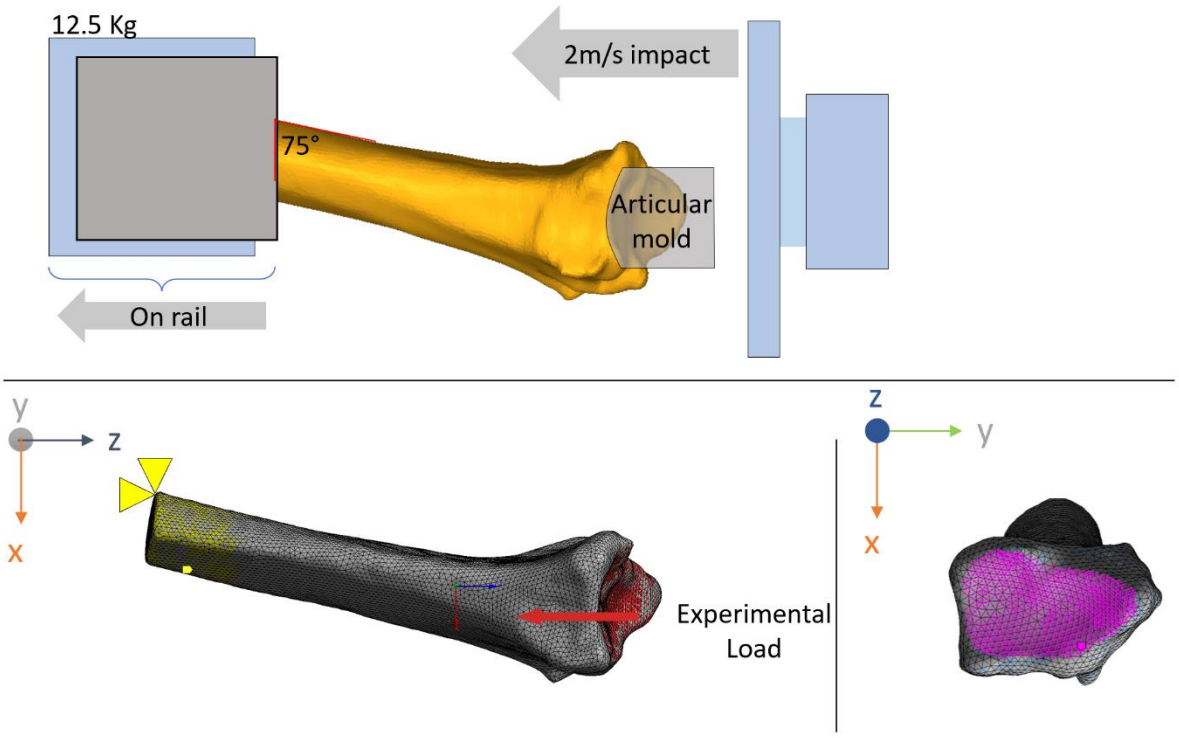
12.5 Kg
2m/s impact
75°
Articular mold
On rail
y
z
x
Experimental Load
z
y
x

Figure 4

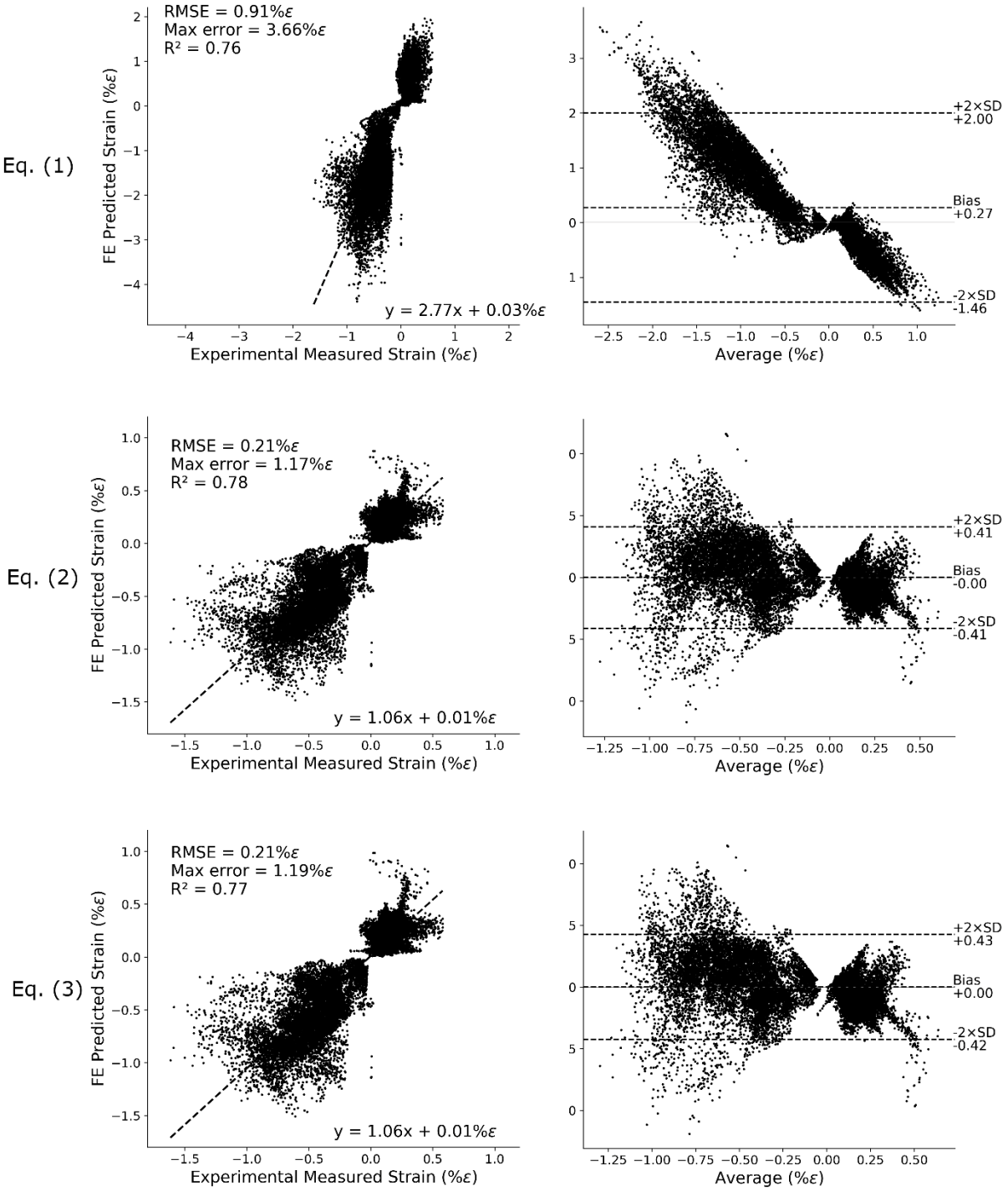
Eq. (1)
RMSE = 0.91%ε
Max error = 3.66%ε
R² = 0.76
y = 2.77x + 0.03%ε
FE Predicted Strain (%ε)
Experimental Measured Strain (%ε)
+2×SD
+2.00
Bias
+0.27
-2×SD
-1.46
Average (%ε)
Eq. (2)
RMSE = 0.21%ε
Max error = 1.17%ε
R² = 0.78
y = 1.06x + 0.01%ε
FE Predicted Strain (%ε)
Experimental Measured Strain (%ε)
+2×SD
+0.41
Bias
-0.00
-2×SD
-0.41
Average (%ε)
Eq. (3)
RMSE = 0.21%ε
Max error = 1.19%ε
R² = 0.77
y = 1.06x + 0.01%ε
FE Predicted Strain (%ε)
Experimental Measured Strain (%ε)
+2×SD
+0.43
Bias
+0.00
-2×SD
-0.42
Average (%ε)

Figure 5

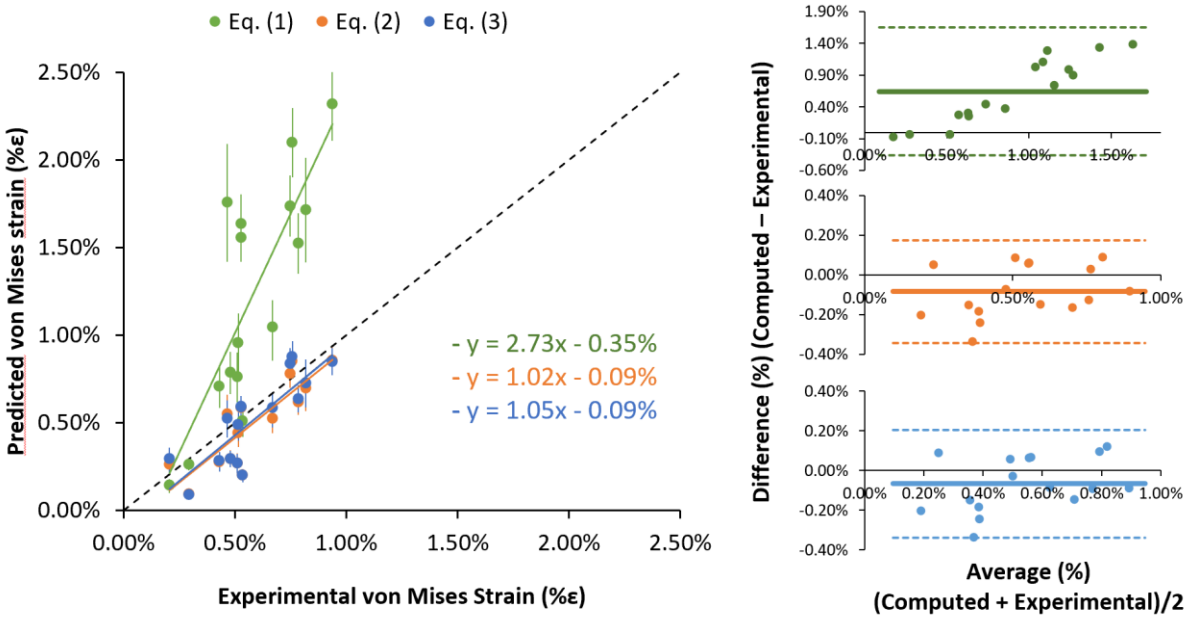

Figure 6

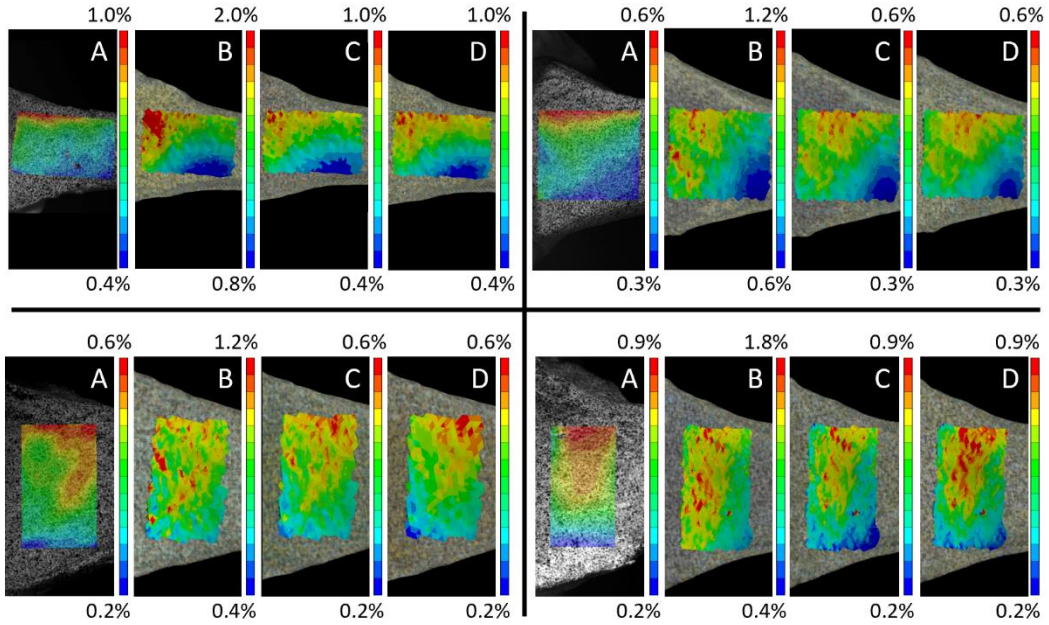

Figure 7

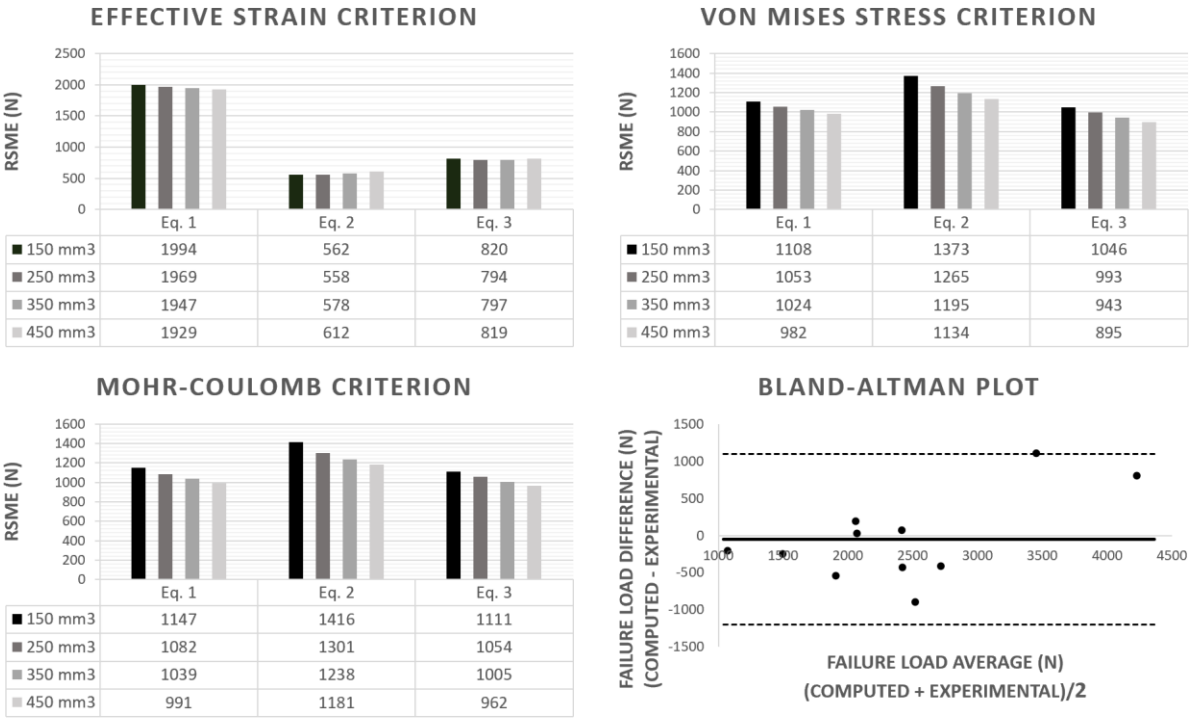

Figure 8

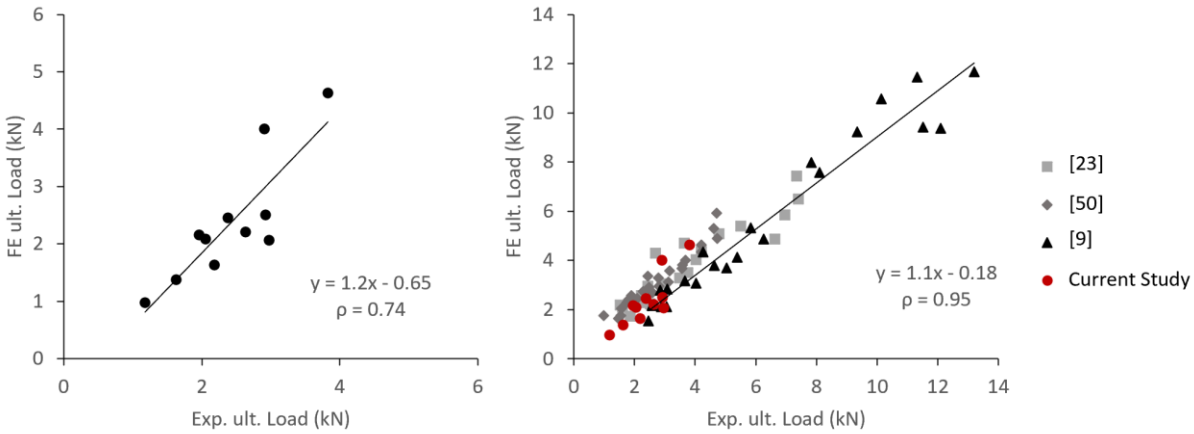

Figure 9.

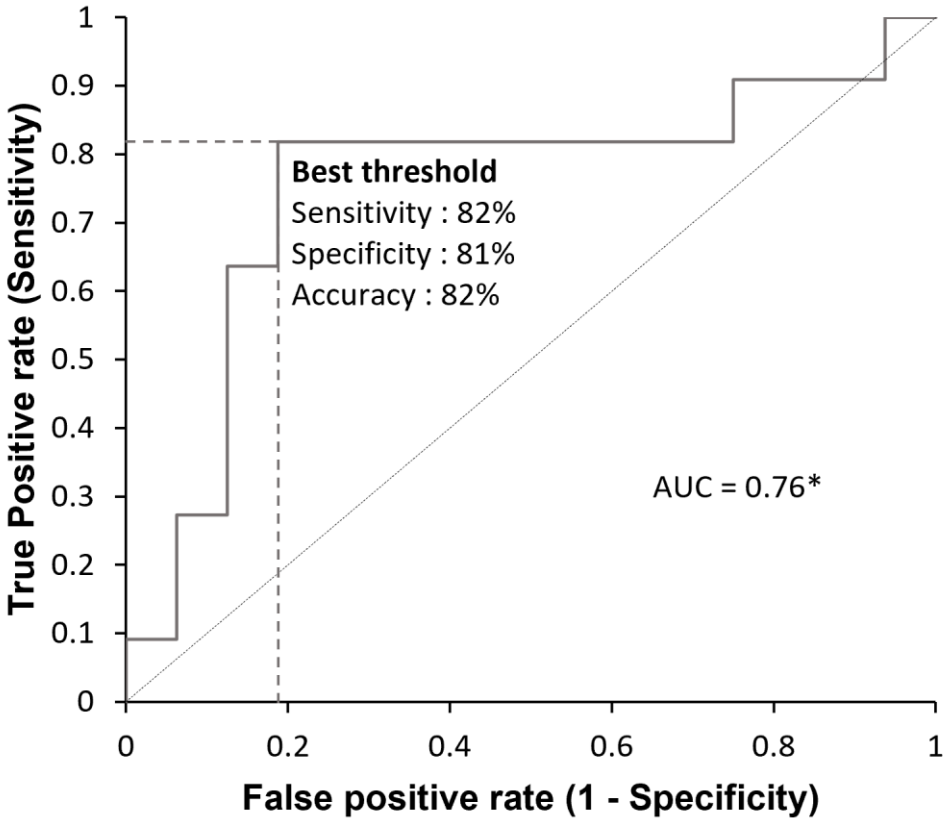
True Positive rate (Sensitivity)
False positive rate (1 - Specificity)
Best threshold
Sensitivity : 82%
Specificity : 81%
Accuracy : 82%
AUC = 0.76*
0
0.1
0.2
0.3
0.4
0.5
0.6
0.7
0.8
0.9
1
0
0.2
0.4
0.6
0.8
1

Supplementary Materials

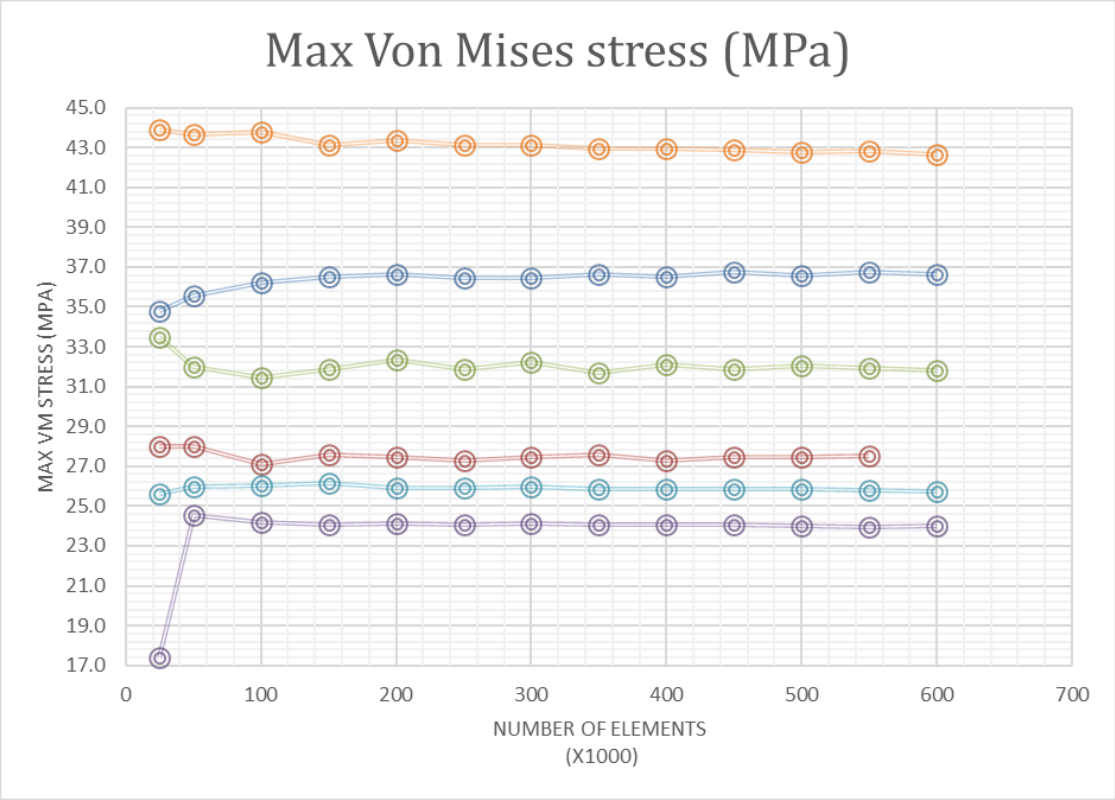

SUPPLEMENTARY Figure 10 : Mesh convergence study on a sub-sample of 6 specimens ranging from 50,000 to 600,000 elements by increments of 50,000. The maximum von Mises stress in the whole model excluding edge effects (excluding the 5% of the highest stress values) was evaluated.

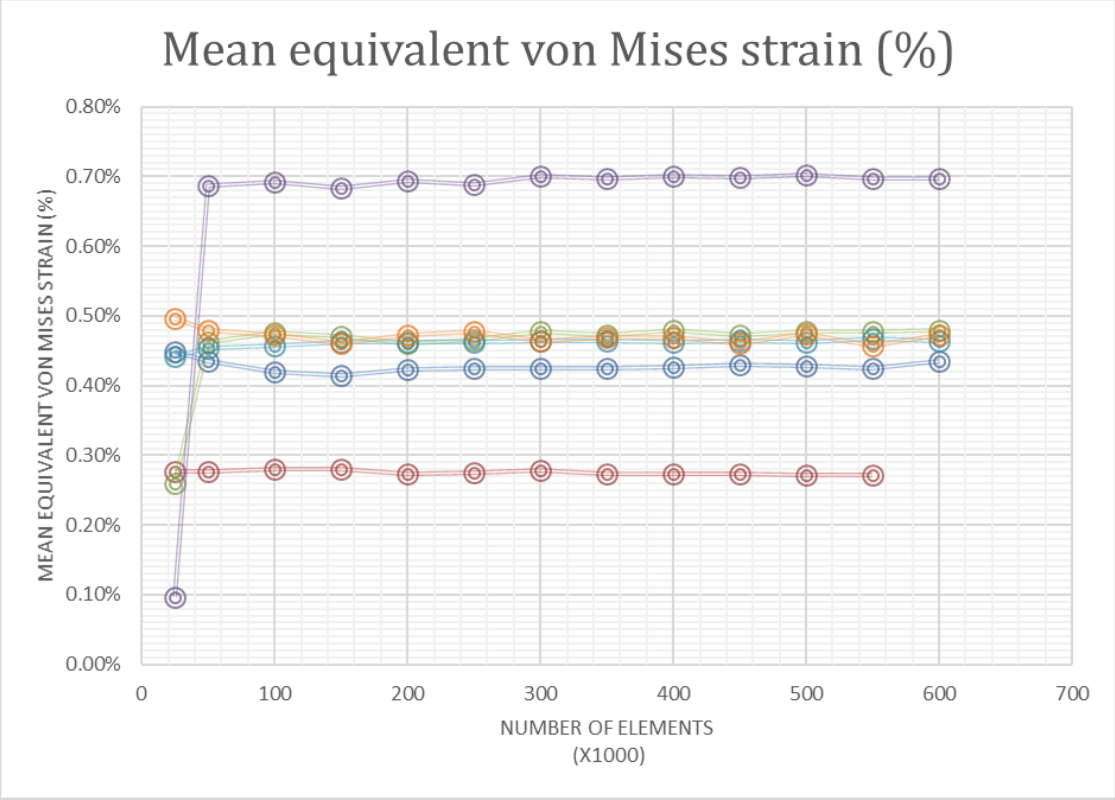

SUPPLEMENTARY Figure 11 : Mesh convergence study on a sub-sample of 6 specimens ranging from 50,000 to 600,000 elements by increments of 50,000. The mean equivalent von Mises strain in a region of interest of the anterior face of the radius was evaluated.

SUPPLEMENTARY Table 4 : For the 16 non fractured specimens: Baseline (mm), distance between cameras. Stereo angle (°) between cameras. Distance to specimen (mm) between cameras and the surface of the radii. This distance was not specifically measured. AOI Hight (mm and px), the long dimension of the analyzed region. Avg projection error (px) after calibration. Facet size or Subset (px) was chosen based on the average confidence interval of the correlation tracking function (sigma estimate ≈0.01 pixels). Step (px, mm), refer to the overlap, was roughly a quarter of the subset in agreement with manufacturer guidelines. Filter size (px, mm) was chosen constants for all specimens. The noise trough time (%def) describes the spread of strain between consecutive images before the impact. Sigma Mean (px), the average error (sigma) of the analyzed images.

Baseline (mm)	Stereo angle (°)	Distance to specimen (mm)	AOI Hight (px)	AOI hight (mm)	avg projection error (px)	Facet Size (Subset, px)	Step (overlap, px)	Step Physical Size (mm)	mm/px ratio	Filter Size	Filter Physical Size (mm)	Noise Through time (%def)	Sigma Mean (error, px)
176	31	540	490	20.7	0.027	41	10	0.43	0.04	15	6.50	0.017%	0.005
176	31	540	509	19.3	0.020	51	13	0.48	0.04	15	7.25	0.024%	0.006
175	31	540	361	25.2	0.026	41	10	0.71	0.07	15	10.71	0.013%	0.004
177	31	540	579	24.1	0.031	53	13	0.55	0.04	15	8.26	0.012%	0.005
177	32	540	298	12.2	0.020	39	10	0.40	0.04	15	5.97	0.012%	0.005
86	26	540	341	9.1	0.017	41	10	0.27	0.03	15	4.09	0.014%	0.024
175	31	540	502	20.1	0.025	37	9	0.37	0.04	15	5.55	0.030%	0.005
175	32	540	411	15.6	0.017	35	9	0.33	0.04	15	4.99	0.032%	0.005
175	31	540	477	18.4	0.019	39	10	0.38	0.04	15	5.65	0.014%	0.005
170	26	540	419	21.7	0.028	41	10	0.53	0.05	15	7.96	0.044%	0.014
175	31	540	473	18.1	0.021	41	10	0.39	0.04	15	5.88	0.008%	0.002
175	31	540	418	17.0	0.022	37	9	0.38	0.04	15	5.63	0.016%	0.005
175	31	540	306	11.9	0.031	35	9	0.34	0.04	15	5.11	0.014%	0.006
176	31	540	480	18.2	0.019	47	12	0.45	0.04	15	6.69	0.011%	0.005
175	32	540	390	15.9	0.018	37	9	0.38	0.04	15	5.67	0.006%	0.005
175	31	540	500	21.2	0.042	37	9	0.39	0.04	15	5.88	0.006%	0.013

SUPPLEMENARY Table 5 : Means predicted failure loads (n=11) with their standard deviation and prediction error of the numerical model for the different failure criteria, contiguous failed elements, and elastic-density relationships.

Experiment (N)	2422 ± 734								
Failure / Volume	Effective Strain Criterion			Von Mises Stress Criterion			Mohr-Coulomb Criterion		
	Eq. 1	Eq. 2	Eq. 3	Eq. 1	Eq. 2	Eq. 3	Eq. 1	Eq. 2	Eq. 3
150 mm^3									
Mean (N)	487	2287	2185	1547	1160	1475	1461	1103	1397
Sd (N)	295	1036	1335	1167	959	851	1098	920	821
RMSE (N)	1994	562	820	1108	1373	1046	1147	1416	1111
Max Err (N)	2650	1101	1317	2007	2216	1792	2049	2245	1857
250 mm^3									
Mean (N)	511	2371	2291	1664	1291	1550	1559	1237	1470
Sd (N)	313	1073	1339	1240	1022	903	1143	978	868
RMSE (N)	1969	558	794	1053	1265	993	1082	1301	1054
Max Err (N)	2574	999	1506	1855	2051	1720	1911	2082	1793
350 mm^3									
Mean (N)	531	2449	2387	1747	1376	1615	1623	1308	1529
Sd (N)	326	1104	1365	1294	1042	921	1167	988	877
RMSE (N)	1947	578	797	1024	1195	943	1039	1238	1005
Max Err (N)	2529	1221	1656	1754	1967	1655	1830	2027	1735
450 mm^3									
Mean (N)	549	2526	2483	1813	1439	1667	1690	1367	1575
Sd (N)	335	1140	1389	1310	1046	916	1192	993	876
RMSE (N)	1929	612	819	982	1134	895	991	1181	962
Max Err (N)	2517	1334	1801	1582	1875	1598	1651	1917	1674